https://doi.org/10.1016/j.cemconres.2023.107340

Effects of Seawater on the Formation and Mechanical Properties of Friedel's Salt Associated with Tricalcium Aluminate

Yamei Cai [a], Yong Tao [a,b,*], Dongxing Xuan [a], Xiaohong Zhu [a], Chi Sun Poon [a,*]

[a] Department of Civil and Environmental Engineering, The Hong Kong Polytechnic University, Hong Kong

[b] State Key Laboratory of Silicate Materials for Architectures, Wuhan University of Technology. Wuhan, Hubei 430070, China

*Corresponding author. Email addresses: yong.tao@polyu.edu.hk (Yong Tao) and cecspoon@polyu.edu.hk (Prof. Chi Sun Poon)

Abstract: This work examines the micromechanical properties of AFm phases formed in seawater and deionized water. As the interlayer SO_4^{2-} in the AFm phase is gradually replaced by Cl^- in seawater, the basal spacing of the AFm crystal narrows, which promotes the packing density of nanocrystals and their indentation modulus and hardness, *i.e.*, Cl-AFm (Friedel's salt) > SO_4-Cl-AFm (Kuzel's salt) > SO_4-AFm (monosulphate). It is found that Friedel's salt formed in seawater feature multiple structural and compositional defects. First, the anions (Cl^-, OH^-, SO_4^{2-}) are bound in the interlayer of Friedel's salt, and the bound OH^- contents have negative relations with the Cl^- concentration in the seawater. Second, the incorporation of Mg ions in the Friedel's salt barely changes its micromechanical properties based on the experimental data and molecular dynamics simulations. Third, when portlandite is present in the seawater, some Ca vacancies would be formed in the Friedel's salt, which would decrease its Young's modulus significantly. This accounts for the decrease in the indentation modulus of Friedel's salt as observed in the experiments. These findings enable us to better understand and control the micromechanical properties of Cl-containing AFm phase formed in seawater-mixed cementitious materials.

Keywords: AFm; Friedel's salt; Seawater; Nanoindentation; Molecular dynamics simulations

1 Introduction

The possible usage of seawater as mixing water in concrete production is gaining increasing interest due to scarce freshwater resources, particularly in coastal areas and isolated islands [1]. The main concern in the use of seawater is the reinforcement corrosion caused by Cl^- ions in seawater. However, referring to plain concrete and fiber-reinforced polymer (FRP) reinforced concrete [2-4], this corrosion problem seems not a limiting factor in applying seawater-mixed concrete.

Previous research on seawater-mixed cementitious materials mainly focused on exploring the effects of seawater on the hydration mechanism, microstructure, and fresh and hardened properties of cement systems and individual clinker phases, such as tricalcium silicate (C_3S) and tricalcium aluminate (C_3A). These studies have pointed out that the relatively high ionic strength of seawater would decrease the activity coefficient of solute ions, such as Ca [5, 6] and SO_4^{2-} species [6], and elevate their corresponding concentrations in the pore solution. This resulted in the accelerating dissolution of C_3S, C_3A, and gypsum [5, 6], which further increased the nucleation rate [7] and precipitation rate [8] of the hydration products. Therefore, the use of seawater in the preparation of cement and concrete can accelerate the early hydration of cement [9-12], shorten the setting time [13, 14], decrease the workability [15-17], refine the pore structure [9, 10], increase the shrinkage [18], and enhance the early compressive strength of the matrix [12, 13, 19].

Referring to the effects of seawater ions on the properties of hydrates, the focus of most published literature is primarily directed towards the hydration product of the silicate phase, namely calcium silicate hydrate gel (C-S-H gel) [20-23]. This is because C-S-H gel constitutes

70-80 % of the volume of Portland cement paste and is the primary contributor to the early strength [24]. However, research on the impact of seawater ions on the structure and properties of the hydration products of the aluminate phase, namely calcium hydroaluminates, is limited. In our previous study, ettringite (AFt), a common calcium hydroaluminate in Portland cement and calcium sulfoaluminate cement, was synthesized in deionized (DI) water and different seawater solutions, and the growth rate, morphologies, structure, and micromechanical properties of different AFt crystals were compared [8]. The results showed that the Mg ions in seawater had a significant influence on the properties of AFt [8].

Apart from AFt, AFm is another common calcium hydroaluminate. Friedel's salt is one type of AFm phase containing Cl^- ions [25-27], and is a new hydrate formed in seawater-mixed concrete through the chemical reaction between Cl^- in seawater and the aluminate phases in cement systems [6, 28, 29]. In cement and concrete, the focus of the previous studies was on the Cl-binding ability of Friedel's salt, which was considered as an effective method of chemical adsorption of Cl^- to reduce the risk of reinforcement corrosion [30, 31].

However, this work focused on the contribution of the formed Friedel's salt to the mechanical properties of seawater-mixed concrete. It is worth noting that the effects of the formed Friedel's salt on the mechanical properties of cementitious materials remain controversial. Wang et al. [9, 32], Li et al. [33] and Mohammed et al. [34] believed that the formation of Friedel's salt could densify the microstructure and improve the integrity of the hydrated cementitious materials, which would further result in higher compressive strength. But Suryavanshi et. al [35] revealed that the refinement of pore structure was due to the modification of C-S-H gel morphology by free-chloride, rather than the deposition of Friedel's salt in the coarse pores. Besides, Li et. al [12] reported that the additional formation of Friedel's salt and ettringite in the seawater-mixed cement mortar could partially compensate for the decrease in strength caused by the lower hydration degree of C_3S in the later ages. Nevertheless,

Zhang et. al [11] stated that the formation of Friedel's salt negatively affected the compressive strength, because of its large size, *i.e.*, several microns, and the hexagonal morphology of Friedel's salt crystal. Its growth could also result in a higher porosity of the matrix. Furthermore, Xiao et. al [36] mentioned that the hydro-expansive property of Friedel's salt and ettringite can cause small cracks inside concrete, which reduce the later-age compressive strength.

In addition to the above diverse viewpoints, comprehensive experimental evaluations on the mechanical properties of Friedel's salt is lacking. This assessment is particularly challenging in the complex cement-based materials, as it is difficult to isolate the individual effects of Friedel's salt from the overall influence of all the hydration phases on the cement matrix.

In this work, the Friedel's salt (Cl-AFm), Kuzel's salt (SO_4-Cl-AFm), and monosulphate (SO_4-AFm) were synthesized using C_3A-seawater, C_3A-gypsum-seawater, and C_3A-gypsum-Milli-Q water, respectively. Then, the micromechanical properties of these phases were compared by the nanoindentation test, evaluating the change of indentation modulus and hardness values when the SO_4^{2-} ions in the AFm phase was gradually occupied by Cl^- ions (from SO_4-AFm to Kuzel's salt and then to Friedel's salt). Furthermore, three other types of Friedel's salts were also synthetized: in NaCl solution, seawater excluding $MgCl_2$, and seawater in the presence of portlandite, respectively. Comparing the micromechanical properties of these four kinds of Friedel's salts, the effect of ions in seawater on the Friedel's salt will be further explored. In addition, the packing density, elemental compositions, and molecular dynamics simulations of different Friedel's salts were also studied to explain the discrepancies in their micromechanical properties. In this study, the synthetic methods of the different AFm phases and the characterization methods of their micromechanical properties were similar to that in the AFt phase work previously reported [8], facilitating comparisons between the effect of seawater on the AFt and AFm phases.

2 Materials and methods

2.1 Materials

A cubic tricalcium aluminate (C_3A) provided by a commercial laboratory was used in this work. The purity and median particle size of C_3A were about 98 % and 7.68 μm, which had been shown in our previous work [8]. In addition, the median particle size of gypsum used was about 22.4 μm, which was also presented in Ref. [6]. Also, calcium hydroxide (CH) with an analytical grade that was purchased from Aladdin Reagent Corporation Limited (Shanghai, China) was adopted.

Simulated seawater (SW) was prepared using the chemical reagents listed in ASTM D1141-98 [37]. The main ions present in the simulated seawater were Cl^- (19.8 g/L), Na^+ (11.0 g/L), SO_4^{2-} (2.8 g/L), Mg^{2+} (1.3 g/L), Ca^{2+} (0.4 g/L), K^+ (0.4 g/L), and HCO_3^- (0.146 g/L).

2.2 Synthesis of different AFm phases

The mix proportions of the suspensions for the experiment are shown in Table 1. Based on the stoichiometric ratio, a gypsum amount of 63.7 % by mass of C_3A was used to produce the monosulphate phase (SO_4-AFm). Milli-Q water was used, and a liquid-to-solid (l/s) ratio of 20 was adopted.

Regarding the synthetic cement hydrates in the seawater system, the amounts of C_3A, gypsum, and seawater were adjusted based on the reaction sequence reported in our previous studies [6, 28]. A C_3A-SW suspension with a liquid/solid (l/s) of 20 was used to synthesize the Friedel's salt in the seawater environment. The l/s of 20 was chosen to provide sufficient Cl^- for the formation of the Friedel's salt, because when the concentration of Cl^- in the pore solution was less than 1.3-1.7 g/L, the residual C_3A would hydrate into hydrogarnet (C_3AH_6) [28]. In addition, in order to produce the Kuzel's salt (S1 and S2 samples in Table 1), the mixtures with a gypsum amount of 35.0 % and 63.7 % by mass of C_3A were used. A l/s of 10 was adopted in

S1 and S2 samples to reduce the total amount of Cl^- introduced by the seawater, which aimed at reducing the formation of Friedel's salt and further promoting the formation of Kuzel's salt.

In order to explore the effect of seawater ions on the structure and properties of Friedel's salt, different types of Friedel's salts were also formed using different starting solutions, *i.e.*, seawater, seawater excluding $MgCl_2$, seawater with CH, and NaCl solution with the same concentration of Cl^- as in seawater (Table 1).

Regarding the synthesis of the above hydration phases, the powder mixture as shown in Table 1 was placed into 50 mL plastic centrifuge tubes. Then, the corresponding solutions were added. After that, these suspensions were rotated at 50 rpm in an end-over-end rotator for 21 d. Subsequently, solid residues were obtained through centrifugation at 10,000 rpm, followed by two rinses with isopropanol. These solids were then transferred to a vacuum oven at 40 °C for 12 h to remove the remaining isopropanol and afterward dried in a vacuum desiccator with silica gel for an additional 2 d at room temperature. Finally, these solids were placed in a desiccator with saturated $CaCl_2$ solution (RH~35%) and a slight vacuum (~ 4 psi) at room temperature for further moisture control.

Table 1. Mix proportion of synthetic samples

Sample name	Gypsum/C_3A [a]	Liquid/Solid [a]	Type of reaction solution
SO_4-AFm	63.7 %	20	Milli-Q water
Fs-SW	0 [b]	20	Seawater
S1	35.0 %	10	Seawater
S2	63.7 %	10	Seawater
Fs-SW-no Mg	0 [b]	20	Seawater excluding $MgCl_2$
Fs-SW+CH [c]	0 [b]	20	Seawater
Fs-NaCl	0 [b]	20	NaCl solution with a same concentration of Cl^- as seawater

[a] mass ratio.

[b] There was no gypsum in reactant.

[c] An appropriate CH was added in C_3A to provide a sat.CH-seawater solution for the synthesis of Friedel's salt. The amount of CH needed was 6.5 g/L seawater after testing a series of pH tests [8].

2.3 Experimental characterizations

2.3.1 Mineralogical composition analysis

The purities of the synthetic hydrates were evaluated using an X-ray diffractometer operated at 45 kV and 200 mA with CuKα radiation (Rigaku SmartLab 9 kW). Before the test, the synthetic samples were co-grinded with 10 % corundum by mass of the total powder. Then, tests were conducted in a range of 5-60 ° 2θ, and the step width and scanning speed were set as 0.02 ° and 2.5 °/min, respectively. Additionally, a qualitative test was recorded in the same 2θ range and the same step width, but the scanning speed was increased to 5 °/min.

Thermogravimetric analysis (TGA) was used to study the phase assemblage of the formed hydrates (PerkinElmer TGA 4000). About 50 mg of samples were placed in a ceramic crucible and heated from 30 °C to 800 °C at a heating rate of 10 °C/min. During the measurement, nitrogen gas was used as a protective gas and the flow rate was 30 mL/min.

2.3.2 Micromechanical properties

A Nano-indenter (Hysitron TI Premier, Bruker) equipped with Scanning Probe Microscopy (SPM) was used to characterize the indentation modulus and hardness of the different synthetic hydrates. The synthetic hydrates with the same mass were placed in a steel die, then disc-shaped specimens with a dimension of ϕ 13 mm × 4 mm were prepared using a hydraulic press at a pressure of 30 MPa for 30 s. Then, the disc-shape specimens were placed in cylindrical moulds and impregnated with epoxy under vacuum conditions. After hardening at 30 °C for 1 d, the

epoxy impregnated samples were released from the moulds and further polished. Firstly, a 1200 grit SiC sanding paper was employed to polish the bottom side of resin samples, aiming to just expose the sample surface by removing a thin layer of resin. A 600 grit SiC sanding paper were used to polish the top side (opposite the sample side) of the resin samples, ensuring the parallelism between the top and bottom surface. Then, the resin samples were successively polished using different polishing cloths and polishing agents (9 μm, 3 μm, and 0.05 μm), and each polishing step lasted at least 30 min. During the process of polishing, ethanol was used as a lubricant as necessary. Between each step, the samples were thoroughly cleaned using ethanol in an ultrasonic bath to eliminate any residue from the sample surface. Once the polishing process was completed, the surface roughness of samples was inspected on an area of 50 μm × 50 μm. The final root-mean-squared (RMS) roughness needed should be less than 50 μm prior to the test, in order to achieve an acceptable roughness associated with the awaited indentation depths [38].

The above polished resin samples were stored in a vacuum desiccator (T=23 ±1 ºC, RH~35%) for another 2 d to evaporate residual chemicals. Then, a nanoindentation test was conducted using a three-sided pyramid Berkovich tip made of diamond (T=23 ±1 ºC, RH~56 %). Even though the relative humidity of about 56 % during the nanoindentation test was higher than that of the desiccator where the samples were stored (~35 %), the bound water content in the SO_4-AFm sample remained unchanged. This was because when the relative humidity ranged from 23 % to 97 %, the bound water content in the SO_4-AFm was still 12 moles [39] (The bound water content in the SO_4-AFm and Friedel's salt samples had been calculated according to the TG test in Fig. S1 in the supplementary material.).

During the measurement process, a trapezoidal loading function was applied: loading for 10 s to the maximal load of 2000 μN, then holding this load for 5 s, and then unloading for 10 s. The crystallographic structure of AFm phases shows an anisotropic elastic tensor. The structure

of AFm phases is composed of stacked $[Ca_2Al(OH)_6]^+$ layers along the c-axis, and different anions and bound water were intercalated into the interlayer spaces. The relatively weak interaction between these interlayers typically results in a lower stiffness along the c-axis. In contrast, the basal plane of AFm crystals demonstrates significantly higher stiffness, resulting in a markedly anisotropic elastic property [40]. Because of the highly anisotropy of AFm phases, the indentation modulus detected in this work could exhibit a specific variation range, which depends on the crystal orientation. In this work, four different regions were selected for each sample, and a 10 × 10 grid with a grid spacing of 10 μm was adopted in each region. Therefore, a total of 400 data points were obtained for each sample, and then the nanoindentation test covered a total area of 32400 μm^2 in each sample. When selecting the test regions, the unhydrated C_3A particles were avoided. The aim of the multi-zone measurement approach in this work was to capture as many different orientations of crystals as possible.

After measurement, the reduced modulus (E_r) and hardness can be obtained. After subtracting the effect of the indenter tip, the indentation modulus (M) was calculated according to the following Equation (2-1) [41].

$$M=\left(\frac{1}{E_r}-\frac{1-\nu_i^2}{E_i}\right)^{-1} \quad (2\text{-}1)$$

Where, E_i and V_i are the parameters of the indenter tip (E_i=1140 GPa and ν_i=0.07 for a diamond tip [42]).

Using the data points of the indentation modulus (M) and indentation hardness (H), the packing density (η = 1 - porosity) of the solid was further calculated following the method reported by Ulm et al. [43]. The specific calculation process is shown in Section S1 in the supplementary material.

2.3.3 Morphology and elemental composition analysis

The morphology of the synthetic Friedel's salt was characterized by using Scanning Electron Microscopy (SEM, TESCAN VEGA3) coupled with an energy-dispersive X-ray spectrometer (EDS). During sample preparation, an ultra-flat polished silicon chip (8 mm × 8 mm) was attached to the microscopy stub with adhesive carbon tape. Then, the suspensions of the synthetic Friedel's salt were first diluted using Milli-Q water and then dropped onto the silicon chips. After vacuum drying and gold coating, the samples were placed inside the SEM chamber, and then the test was performed in a resolution scan mode with an accelerating voltage of 20 kV and a working distance of ~ 10 mm.

Furthermore, selected area electron diffraction was used to analyse the synthetic Friedel's salt samples by a transmission electron microscope (TEM, JEM-2100F, JEOL). TEM was operated at an acceleration voltage of 200 kV. Droplets of suspension containing the synthetic Friedel's salt samples were ultrasonically dispersed in isopropanol. Then, 10 μL of the dispersed suspension was deposited onto the surface of a 300-mesh carbon-coated copper grid. After that, this copper grid was dried in a vacuum desiccator before the TEM test.

After the nanoindentation test, the epoxy impregnated samples were carbon coated and used to analyse their elemental compositions using the EDS test in the backscattered electron (BSE) mode of the SEM and at a magnification of × 4000. For each region, 10 points with a spacing of ~ 20 μm were analysed, and data of a total of at least 100 points were collected for each sample. During the selection of interested regions, unhydrated C_3A was avoided.

2.3.4 pH value

The pH values of the solution of the suspension samples were recorded using a pH meter (SevenExcellence, METTLER TOLEDO). The Friedel's salt samples prepared after hydration of the C_3A samples for 10 min, 30 min, 1 h, 2 h, and 1d were centrifugated at 10,000 rpm for

5 min. The supernatant was collected after passing through a 0.45 μm membrane filter. The pH value was measured immediately.

2.3.5 Particle size distribution

The particle size distributions of the synthetic Friedel's salts after 21 d hydration were measured using dynamic light scattering with a Zetasizer analyser (Nano-ZS90, Malvern Co., UK).

2.4 Molecular dynamics simulations

According to elemental analysis (Section 3.2.4), Friedel's salt formed in the seawater feature atomic defects such as atomic replacement and vacancies. To understand the potential influence of these defects on the elastic properties of the Friedel's salt, the elastic moduli of the Friedel's salt with Mg substitutions, Ca ion vacancies, and combined defects were estimated using molecular dynamics simulations. The pristine unit cell of the Friedel's salt was obtained from previous experiments [44]. As shown in Fig. 1, Mg ions and/or Ca vacancies were introduced into the supercell of 3 × 4 × 2 by randomly substituting and/or deleting Ca ions. Four types of defective nanocrystal models of Friedel's salt were constructed: Type.1: the Friedel's salt with 10 at.% Ca substituted by Mg; Type.2: the Friedel's salt with 5 at.% Ca vacancies; Type.3: the Friedel's salt with 10 at.% Ca vacancies; Type.4: the Friedel's salt with 10 at.% Ca vacancies and 5 at.% Ca substituted by Mg. In order to maintain the electroneutrality of the model, the anions (Cl^-) neighbouring the Ca vacancies were removed for charge balance. Considering the different Ca sites, random substitutions and/or deletion involve a huge number of possible combinations. Therefore, for each type of defect modelled, energy minimization was performed on 3000 preliminary models and 9 configurations with the lowest potential energy were screened out. The elastic moduli were averaged as a representative of the defects. The

selected configurations were first fully relaxed under an isothermal-isobaric ensemble at 300 K and zero pressure for 2 ns before being adopted to calculate the elastic tensor. The molecular dynamics simulation used the Nose-Hoover thermostat and barostat with a timestep of 1 fs. The bulk, shear, Young's moduli, and Poisson's ratio were calculated based on the Voigt-Reuss-Hill approximation [45]. All the simulations were implemented with the LAMMPS [46, 47] software using the AFFF [48] force field developed explicitly for the ettringite and monosulfoaluminate phases.

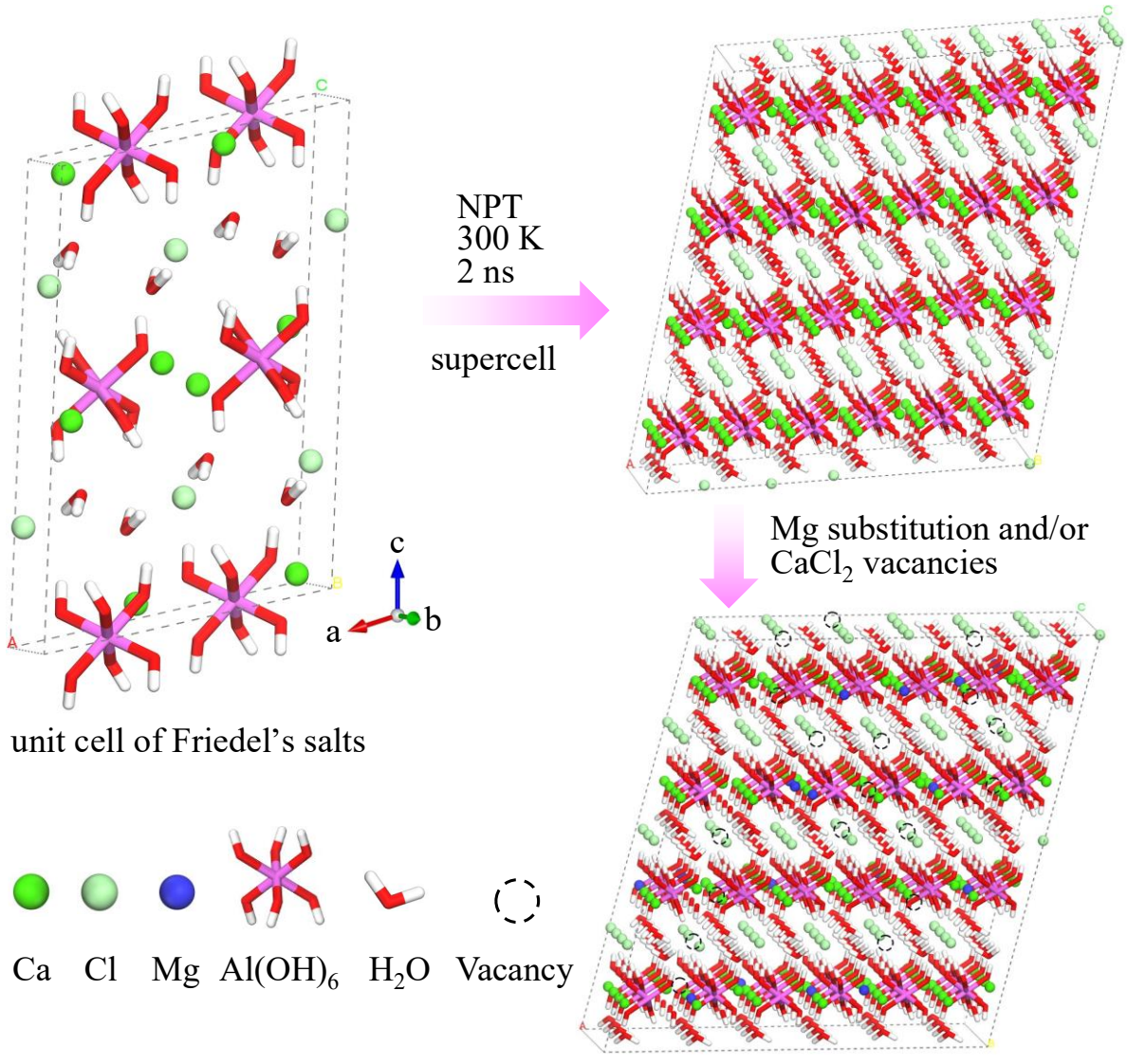

Fig. 1 Schematic diagram of constructing defected nanocrystal models of Friedel's salt.

3 Results and discussions

3.1 Micromechanical properties of different AFm phases formed in seawater

When seawater was used as the mixing water, the types of Cl-containing AFm produced depended on the concentration of Cl^- in the reaction systems, *i.e.*, generating the Friedel's salt at a higher concentration of Cl^- and Kuzel's salt at a lower concentration of Cl^- [49]. As for the seawater-mixed cementitious materials, the effect of Cl-containing AFm formed on the micromechanical properties of the matrix was explored, by designing and forming three different AFm phases, *i.e.*, Cl-AFm, SO_4-Cl-AFm and SO_4-AFm.

3.1.1 Mineralogical compositions

The qualitative XRD patterns and quantitative results of the different synthetic hydration phases are shown in Fig. 2 and Table 2, respectively. It is noted that the purity of the Friedel's salt synthesized in seawater (Fs-SW) was about 94 %. Besides, the purity of monosulphate synthesized in Milli-Q water (SO_4-AFm) was 90 %, and the remaining phase was AFt. Additionally, the mixtures containing different hydration phases were also determined, and the compositions of S1 and S2 were approximately 9 % AFt + 23 % Fs + 64 % Ks, and 43 % AFt + 27 % Fs + 24 % Ks, respectively. By comparing S1 with S2, it was observed that the amount of Friedel's salt was comparable in these two samples. However, the S1 sample had a relatively larger amount of Kuzel's salt, and the S2 sample had more AFt. Therefore, the S1 sample was also termed the rich-Kuzel's salt sample in the following sections.

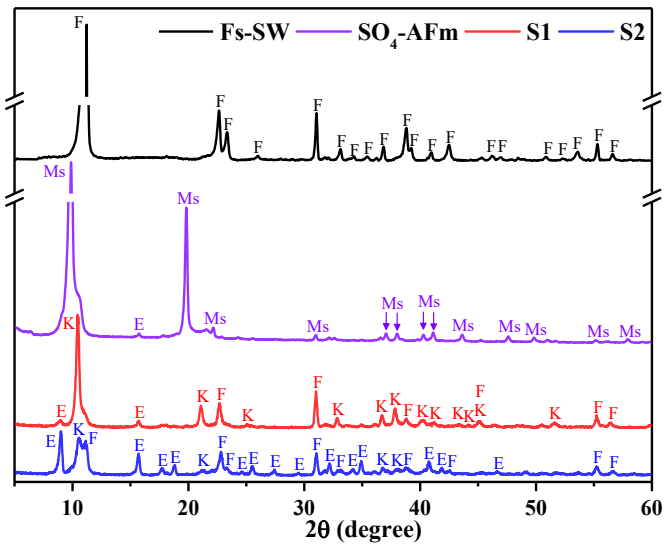

Fig. 2 Qualitative XRD patterns of synthetic different phases. Compared the XRD peak position of SO_4-AFm with the corresponding data in Ref. [39], and according to the TGA data in Fig. S1 in the supplementary material, it can be determined that the bound water content in the monosulphate was 12 moles. Thus, it was referred to as monosulphate-12. (F: Friedel's salt, E: ettringite (AFt), Ms: monosulphate-12, K: Kuzel's salt)

Table 2. Quantitative analysis results for synthetic different phases

Sample name	SO_4-AFm	AFt	Friedel's salt	Kuzel's salt	C_3AH_6	C_3A	amorphous
SO_4-AFm	90.0	9.9	-	-	-	0.1	-
Fs-SW	-	-	93.7	-	1.2	3.1	2.0
S1	2.2	9.1	22.9	64.0	-	1.8	-
S2	1.5	42.9	26.7	24.4	-	2.6	1.9

3.1.2 Micromechanical properties

The frequency plots of indentation modulus and hardness of the different synthetic hydration phases are shown in Figs. 3 (a) and 3 (b). As reported by Ulm et.al [43], the indentation modulus and hardness of hydration phases were directly proportional to their packing densities. Thus, the relationship of the indentation modulus and hardness with the packing density are displayed

in Figs. 3 (c) and 3 (d), and their mean packing density (η), intrinsic stiffness (m_s) and intrinsic hardness (h_s) are illustrated in Table 3. Among them, the intrinsic stiffness and intrinsic hardness are defined as the corresponding indentation modulus and hardness when the packing density is approaching to 1 as shown in Figs. 3 (c) and 3 (d), *i.e.*, $m_s = \lim_{\eta=1} M$ and $h_s = \lim_{\eta=1} H$.

As for the indentation modulus in Fig. 3 (a), the Fs-SW sample had a relatively larger modulus (9 - 22 GPa), followed by the rich-Kuzel's salt sample (S1 sample, 7-15 GPa) and the SO_4-AFm sample (1.5-7.5 GPa). By contrast, the modulus values of these three samples were all lower than that of the SW-AFt sample. Because the S2 sample contained 43 % AFt phase, its modulus values were marginally larger than that of the Fs-SW sample but slightly lower than that of the SW-AFt sample as shown in Fig. 3 (a). Comparing Fig. 3 with Table 3, the relatively larger packing densities and intrinsic stiffness of the hydration phases could be responsible for their relatively higher indentation modulus. In other words, the packing density and intrinsic stiffness values of the different synthetic hydration phases followed a similar trend as their corresponding indentation modulus values, *i.e.*, the SW-AFt sample (η=0.89, m_s=25.42 GPa) > the S2 sample (η=0.85, m_s=23.46 GPa) > the Fs-SW sample (η=0.84, m_s=22.11 GPa) > the rich-Kuzel's salt sample (S1 sample, η=0.77, m_s=19.97 GPa) > the SO_4-AFm sample (η=0.65, m_s=15.48 GPa).

In comparison with the indentation modulus of the different phases in Fig. 3 (a), the hardness values in Fig. 3 (b) also followed a similar trend: the Fs-SW sample > the rich-Kuzel's salt sample (S1 sample) > the SO_4-AFm sample. But an obvious difference was that the hardness value of the SW-AFt sample was slightly lower than that of the Fs-SW sample, which also resulted in a decrease in the hardness of the S2 sample that contained 43 % SW-AFt phase compared with the Fs-SW sample. This could be attributed to the lowest intrinsic hardness of the SW-AFt sample compared with other AFm phases as shown in Table 3.

Overall, it can be concluded that the Cl-bearing AFm had a relatively larger indentation modulus and hardness than the SO_4-bearing AFm, *i.e.*, Cl-AFm (Friedel's salt) > SO_4-Cl-AFm (Kuzel's salt) > SO_4-AFm (monosulphate). This could be related to the different anion radii present in the interlayer of Ca-Al layered double hydroxide of AFm structure, *i.e.*, SO_4^{2-} (0.215 nm) > Cl^- (0.181 nm) [50]. When the SO_4^{2-} in this interlayer was gradually replaced by Cl^-, the interlayer spacing would be reduced, *i.e.*, the basal spacing would decrease from 8.97 Å (monosulphate-12) to 8.43 Å (Kuzel's salt) to 7.87 Å (Friedel's salt). (These calculated basal spacing from XRD data coincided with those in reported literature: 8.96 Å, 8.40 Å and 7.82 Å for monosulphate-12, Kuzel's salt and Friedel's salt respectively [51].) Consequently, the packing density of the AFm phases was increased correspondingly (Table 3), which would further lead to a rise in their indentation modulus and hardness values. A comparable phenomenon was also reported in the tobermorite structure: the elastic modulus of tobermorite increased with the decrease of its interlayer distance, *i.e.*, from 14 Å to 11 Å to 9 Å [52-54]. This is mainly because a shorter interlayer spacing distance increased the interaction between the adjacent layers [52].

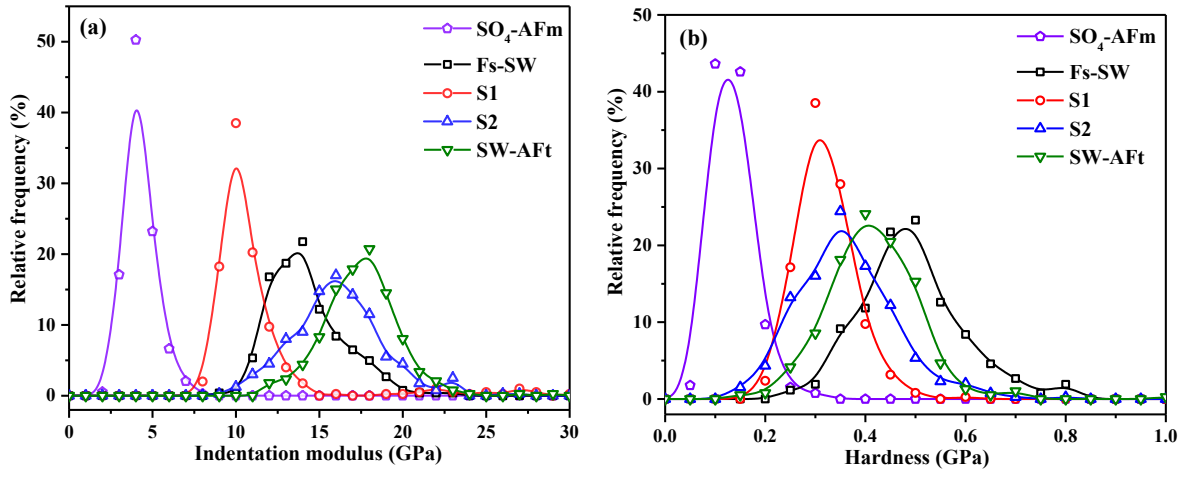

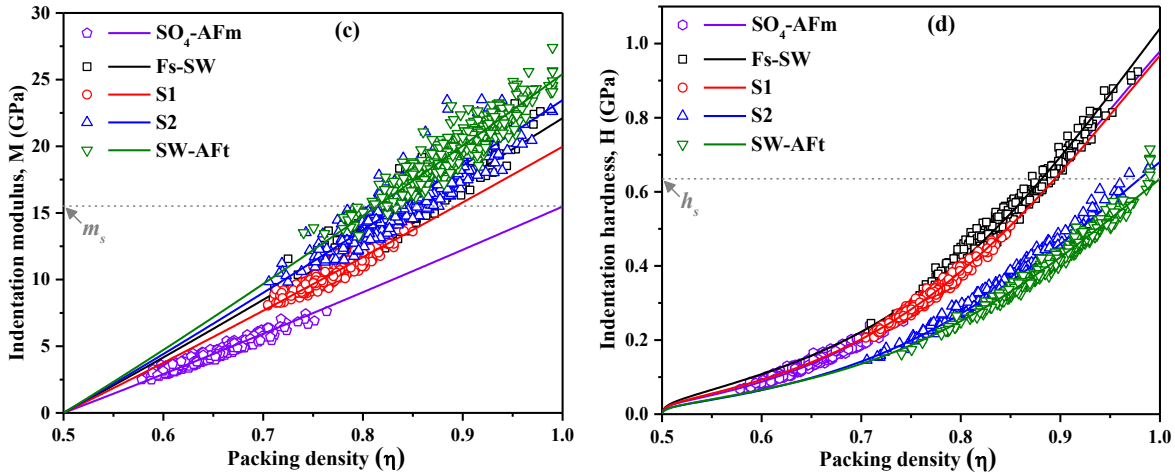

Fig. 3 Frequency plots of indentation modulus (a) and hardness (b) for different hydration phases. Based on the nanoindentation data, the scaling relations of indentation modulus (M) and hardness (H) with the packing density (η) of different synthetic products were calculated: (c) is M-η scaling and (d) is H-η scaling. 'SW-AFt' in the legend denotes the AFt was synthesized in seawater solution, and the preparation and properties characterization of the SW-AFt sample had been displayed in our previous study [8].

Table 3. Mean packing density (Mean η), intrinsic stiffness (m_s) and intrinsic hardness (h_s) for different synthetic hydration phases.

Sample ID	Mean η (%)	m_s (Gpa)	h_s (Gpa)
SO_4-AFm	0.65	15.48	0.98
Fs-SW	0.84	22.11	1.04
S1	0.77	19.97	0.97
S2	0.85	23.46	0.68
SW-AFt	0.89	25.42	0.63

3.2 Effects of seawater ions on the properties of Friedel's salt

Even though NaCl is a major component of seawater, many other ions are also present in seawater, *e.g.*, Mg^{2+}, Ca^{2+}, K^{+}, SO_4^{2-}. As reported, Friedel's salt belongs to a calcium-aluminium layered double hydroxide (Ca-Al LDH) phase [28]. Some cations could be intercalated into the hydroxide layers of the LDH phase through isomorphic substitution [55, 56], and the associated anions could be adsorbed in the interlayer of LDH [57]. Thus, it is necessary to examine the influence of the different ions in seawater on the properties of Friedel's salt. Additionally, considering that Friedel's salt in the seawater-mixed cementitious material would be precipitated after the consumption of gypsum, at that time, a large amount of portlandite would be produced from the hydration of C_3S. Thus, the environment of forming the Friedel's salt in the cementitious material can be simplified as a pore solution with a saturated calcium hydroxide (sat. CH). In this study, a suitable amount of CH was added to simulate the condition of sat.CH, and then the properties of Friedel's salt formed in this seawater-sat.CH environment were further investigated.

Based on the discussion above, four different Friedel's salt samples were designed and compared, *i.e.*, Friedel's salts synthesized in seawater (Fs-SW), $MgCl_2$-free seawater (Fs-SW-no Mg), seawater with sat.CH (Fs-SW+CH), and NaCl solution with the same concentration of Cl^- as seawater (Fs-NaCl sample). The purities of the synthetic Fs-SW, Fs-SW-no Mg, Fs-SW+CH and Fs-NaCl samples were about 94 %, 88 %, 93 % and 86 %, respectively. Their qualitative XRD patterns and quantitative analysis are displayed in Fig. S2 (a) and Table S1 in the supplementary material.

3.2.1 Formation process of Friedel's salt in seawater

Compared with the NaCl solution, the Mg^{2+} and SO_4^{2-} present in seawater also involve in the hydration reactions of C_3A. Thus, these reaction products relevant to the Mg^{2+} and SO_4^{2-} ions were clarified first.

The phase evolution with time of the Friedel's salt samples formed in seawater with and without CH are shown in Figs. 4 (a) and 4 (b). As for the Fs-SW sample in Fig. 4 (a), within the first 30 min of hydration, two small and broader peaks at around 11.1 ° and 31.0 ° were observed, which were very close to the peak positions of Friedel's salt (11.2 ° and 31.1 °). At 1 h, the intensity of these two peaks slightly increased. At 2 h, ettringite and Friedel's salt were detected. Until 1 d, an abundant amount of Friedel's salt and less amount of unhydrated C_3A were observed, while ettringite disappeared. When CH was present (Fig. 4 (b)), no new reaction products were observed in the first 2 h of hydration, indicating a delayed reaction compared to the Fs-SW sample. This phenomenon was in agreement with those reported in the C_3A-CH system [58] and the C_3A-gypsum-CH reaction system [6]. This retardation could be attributed to the surface deposition of CH on the C_3A particles [59], which might impede the dissolution of C_3A. After 1 d of hydration, a large amount of Friedel's salt was precipitated (Fig. 4 (b)).

The evolution of the pH value of the Fs-SW and Fs-SW+CH samples is displayed in Fig. 4 (c). There was a reduction of pH value in the first 30 min of hydration, which had been proven to be related to the consumption of OH^- by the Mg ions of seawater in a previous study [6]. (See the concentration evolution of Mg ions in the Fs-SW and Fs-SW+CH samples with reaction time in the Fig. S3 in the supplementary material). After 30 min, a continuous increase in pH value was found. In addition, TG/DTG was used to further explore the reaction products of the Fs-SW and Fs-SW+CH samples at 30 min, and the results are displayed in Fig. 4 (d). It can be found that the main phase in the Fs-SW and Fs-SW+CH samples was the layered double hydroxide phase (LDH), *i.e.*, probably Ca-Al LDH (Friedel's salt in this case) or Mg-Al LDH

or Ca-Mg-Al LDH. The decomposition peaks of this LDH phase can be summarized as [8, 60-63]: (i) the removal of the physically adsorbed water and interlayer water at around 130 °C, (ii) the dehydroxylation of the hydroxide layer at around 270 °C and 320 °C, (iii) the phase transformations at around 670 °C, such as the recrystallisation of lime (CaO) and mayenite ($Ca_{12}Al_{14}O_{33}$) for Ca-Al LDH or the recrystallisation of periclase (MgO) and spinel ($MgAl_2O_4$) for Mg-Al LDH [64, 65]. When the Fs-SW and Fs-SW+CH samples at 30 min were calcinated at 1000 °C for 2 h, only mayenite, periclase and lime were detected, besides the remaining C_3A (Fig. S4 (a) in the supplementary material). This can be inferred that the LDH phase formed could be a Ca-Al LDH, but a little Mg ions could also be inserted into the principal layer ($[Ca_2Al(OH)_6]^+$) to form a Ca-Mg-Al LDH, since only periclase and no spinel was detected in the decomposition product at 1000 °C. Besides, the peak at around 670 °C could also be ascribed to the decomposition of carbonates, because 0.146 g/L HCO_3^- was included in the simulated seawater. Additionally, a dehydroxylation peak of CH at around 418 °C was noted in the Fs-SW+CH sample due to the incorporation of CH.

In summary, at the beginning of hydration, the dissolution of C_3A would release $Al(OH)_4^-$, Ca^{2+} and OH^-. Then, the Ca^{2+} dissolved or the Mg^{2+} in seawater would be co-precipitated with the $Al(OH)_4^-$ to form Ca-Al LDH (Friedel's salt) and/or Ca-Mg-Al LDH [66], and OH^- was also consumed in this process. When CH was present, the Mg^{2+} ions in seawater formed brucite reported in the C_3A-gypsum-seawater system [8]. But brucite was not detected in the TG data in this C_3A-seawater system without gypsum. Therefore, it was inferred that the Mg^{2+} ions could react with $Al(OH)_4^-$, OH^- and Ca^{2+} dissolved from C_3A to form a Ca-Mg-Al LDH phase (Fig. 4 (d)).

As for SO_4^{2-} present in seawater, it would react with C_3A to form ettringite initially. Then, this ettringite would be transformed to monosulphate (SO_4-AFm) when the SO_4^{2-} concentration was depleted. After that, this SO_4-AFm was further converted to Friedel's salt in the presence

of Cl^- in the seawater (See Fig. S4 (b) in the supplementary material). The transformation from ettringite to Friedel's salt can be seen in the phase evolution of the Fs-SW sample (Fig. 4 (a)), but it was not captured in the Fs-SW+CH sample due to its relatively slower reaction rate than the Fs-SW sample.

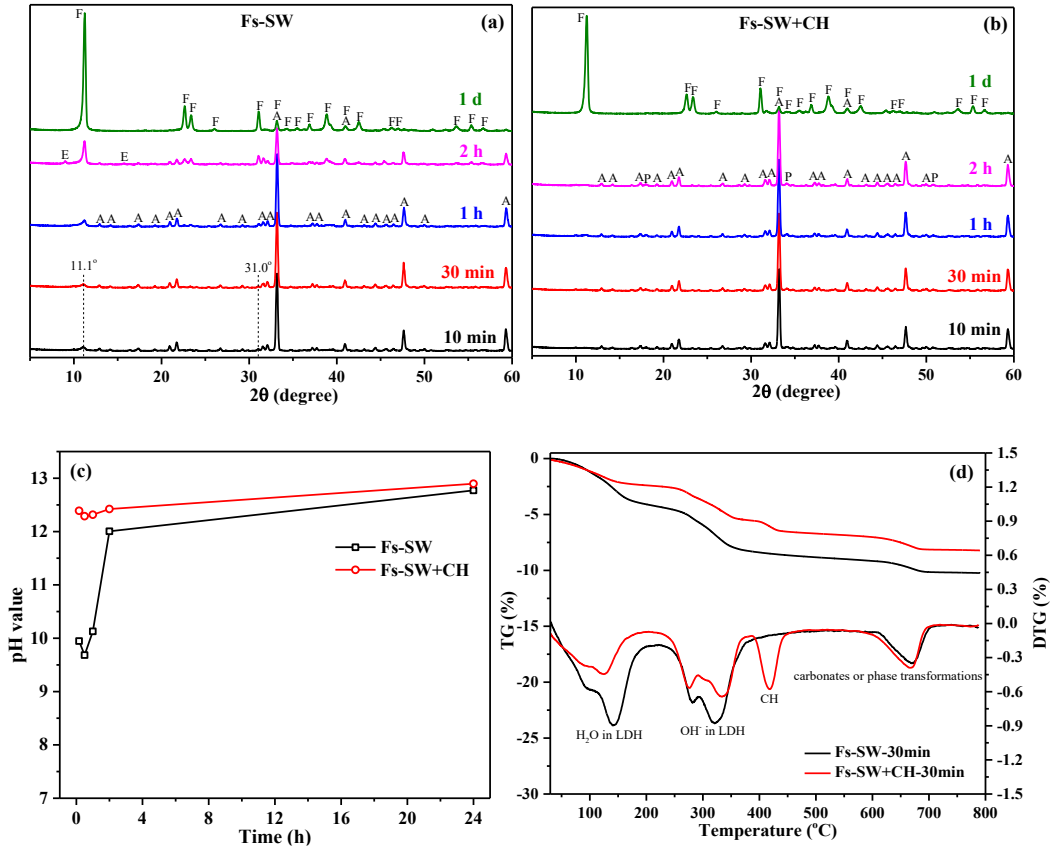

Fig. 4 (a) and (b) XRD patterns of the Fs-SW and Fs-SW+CH samples at different reaction times. A = C_3A, F = Friedel's salt, E = ettringite (AFt), P = calcium hydroxide (CH). (c) pH value evolution for the Fs-SW and Fs-SW+CH samples. (d) TG/DTG curves of the Fs-SW and Fs-SW+CH samples at 30 min of hydration.

3.2.2 Morphology

The morphologies and selected area electron diffraction (SAED) patterns of different synthetic Friedel's salt are displayed in Fig. 5. It is noted that Friedel's salt showed an

anisotropic morphology, and the ab faces of Friedel's salt tended to be parallel to the substrate. This tendency was particularly noticeable in the Fs-SW+CH sample (Fig. 5 (h)). Besides, the Fs-SW sample appeared to have a relatively less regularity and rougher surface in Figs. 5 (a) - 5 (b). By contrast, the Friedel's salt formed in the $MgCl_2$-free seawater (Fs-SW-no Mg sample), seawater with CH (Fs-SW+CH sample) and NaCl solution (Fs-NaCl sample), were well-defined hexagonal shaped platelets with a smooth surface. These relatively rough surfaces for the Fs-SW sample could be related to the relatively larger fluctuation of the initial pH value in Fig. 4 (c). It had been reported that the LDH crystals with rough surfaces were formed in solutions with a variable pH value, in contrast, the well-formed hexagonal crystals were normally precipitated from a constant-pH solution [67, 68]. Besides, the SAED pattern of different Friedel's salts showed hexagonally arranged diffraction spots, indicating the nature of the single-crystal structure. Compared with the Fs-NaCl sample (Fig. 5 (l)), the spots detected in the Fs-SW sample in Fig. 5 (c) were less intense and relatively indistinct, implying a relatively lower crystallinity of Friedel's salt [69]. This could also be reflected in the relatively lower and wider characteristic XRD peaks of the Fs-SW sample shown in Fig. S2 (b). By contrast, when CH was present, the crystallinity of Friedel's salt formed in seawater was improved (Fig. 5 (i)), which indicated that the crystallinity of synthetic Friedel's salt was pH-dependent.

In addition, the particle size of the Friedel's salt in the Fs-SW+CH sample (Figs. 5 (g) - 5 (h)) was relatively smaller than that in other samples, and this was also supported by the particle size distribution results of the Friedel's salt samples (Fig. S5 in the supplementary material). This particle size was dependent on the OH^- concentration of the reaction solution. It has been reported that the presence of CH in the C_3A-water system would result in the formation of relatively smaller hexagonal hydro-aluminate crystals [58, 70].

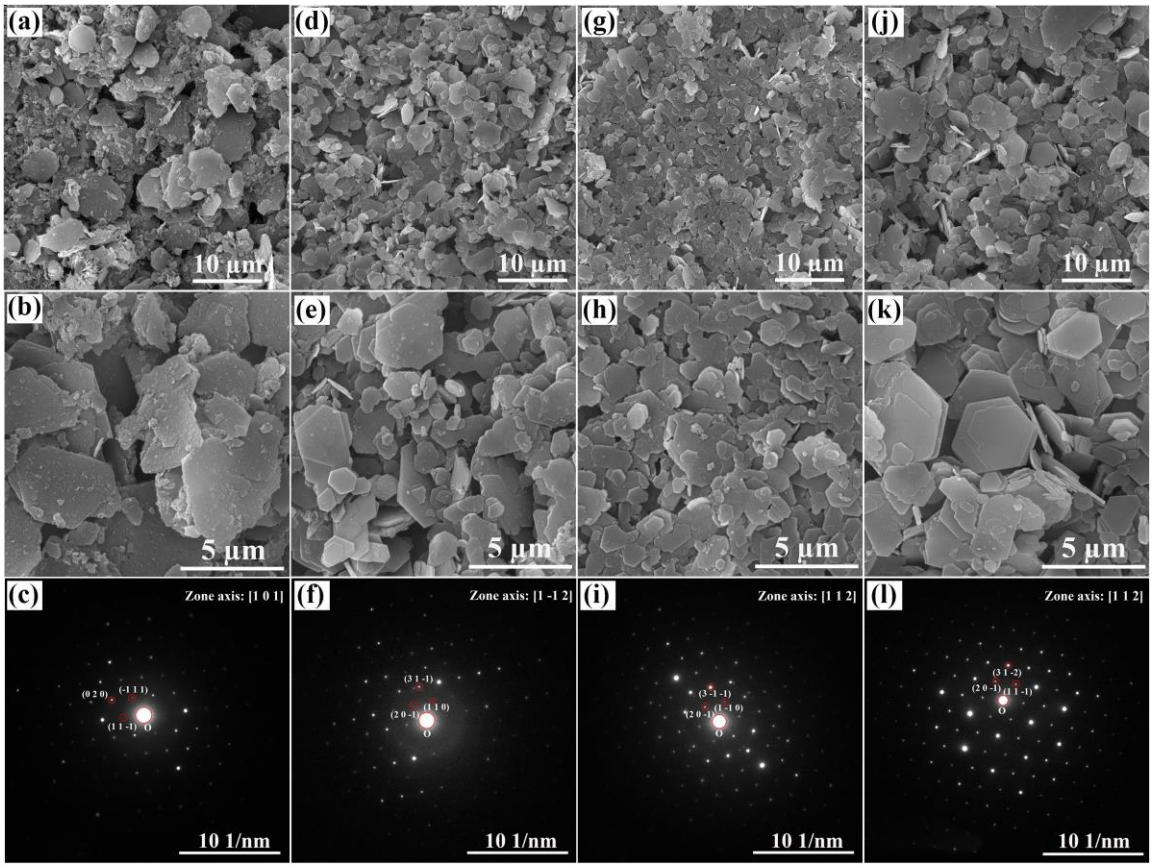

Fig. 5 SEM images and TEM selected area electron diffraction (SAED) pattern ((c), (f), (i), (l)) of the synthetic Fs-SW ((a)-(c)), Fs-SW-no Mg ((d)-(f)), Fs-SW+CH ((g)-(i)) and Fs-NaCl ((j)-(l)) samples. The crystal planes and zone axis in the SAED pattern were indexed to the structure of Friedel's salt.

3.2.3 Micromechanical properties

The indentation modulus and hardness of the synthetic different Friedel's salt are shown in Figs. 6 (a) and 6 (b). Furthermore, the scaling relations of the indentation modulus (M) and hardness (H) with the packing density (η) of these Friedel's salt samples are presented in Figs. 6 (c) and 6 (d), and their mean packing density (η), intrinsic stiffness (m_s), and intrinsic hardness (h_s) are given in Table 4.

From Fig. 6 (a), the indentation moduli for the Friedel's salt formed in seawater (Fs-SW: 9.5-23.8 GPa), seawater excluding $MgCl_2$ (Fs-SW-no Mg: 8.0-21.3 GPa), and NaCl solutions

(Fs-NaCl: 9.5-19.8 GPa) were similar. This was also favoured by the minimal divergence of their packing densities and intrinsic stiffness in Table 4. By contrast, in the presence of calcium hydroxide (CH), the indentation modulus of the Friedel's salt formed in seawater tended to be the lowest, ranging from ~ 4.3 - ~ 12.8 GPa. Meanwhile, its packing density and intrinsic stiffness were relatively lower than the other Friedel's salt samples in Table 4.

Regarding the hardness value in Fig. 6 (b), the Fs-SW+CH sample had the lowest hardness values, *i.e.*, 0.06-0.5 GPa, which was related to its relatively lower packing density and intrinsic hardness compared to the other Friedel's salt samples (Table 4). By contrast, the Fs-SW and Fs-SW-no Mg samples had a modest hardness value, and the hardness value of the Fs-SW sample was slightly larger than that of the Fs-SW-no Mg sample. Additionally, the Fs-NaCl sample had the highest hardness values, *i.e.*, 0.28-0.95 GPa, which could be explained by its relatively higher intrinsic hardness as shown in Table 4, *i.e.*, a 28 % higher intrinsic hardness than those of the Fs-SW and Fs-SW-no Mg samples was noted.

In comparison to other Friedel's salt samples, the Fs-SW+CH crystals exhibited a notable tendency for a great number of ab faces to align parallel to the substrate (Fig. 5). This implied that a larger proportion of the nanoindentation points were likely to occur in the basal plane, which possessed a higher stiffness, rather than in the interlayer position with a lower stiffness. This was also embodied in the relatively concentrated indentation modulus and hardness values for the Fs-SW+CH sample depicted in Figs. 6 (a) and 6 (b). However, it should be noted that the modulus and hardness of the Fs-SW+CH sample remained comparatively lower. This indicates that the relatively lower micromechanical property of the Fs-SW+CH sample was dependent more on its intrinsic characteristics, rather than the effect of crystal anisotropy.

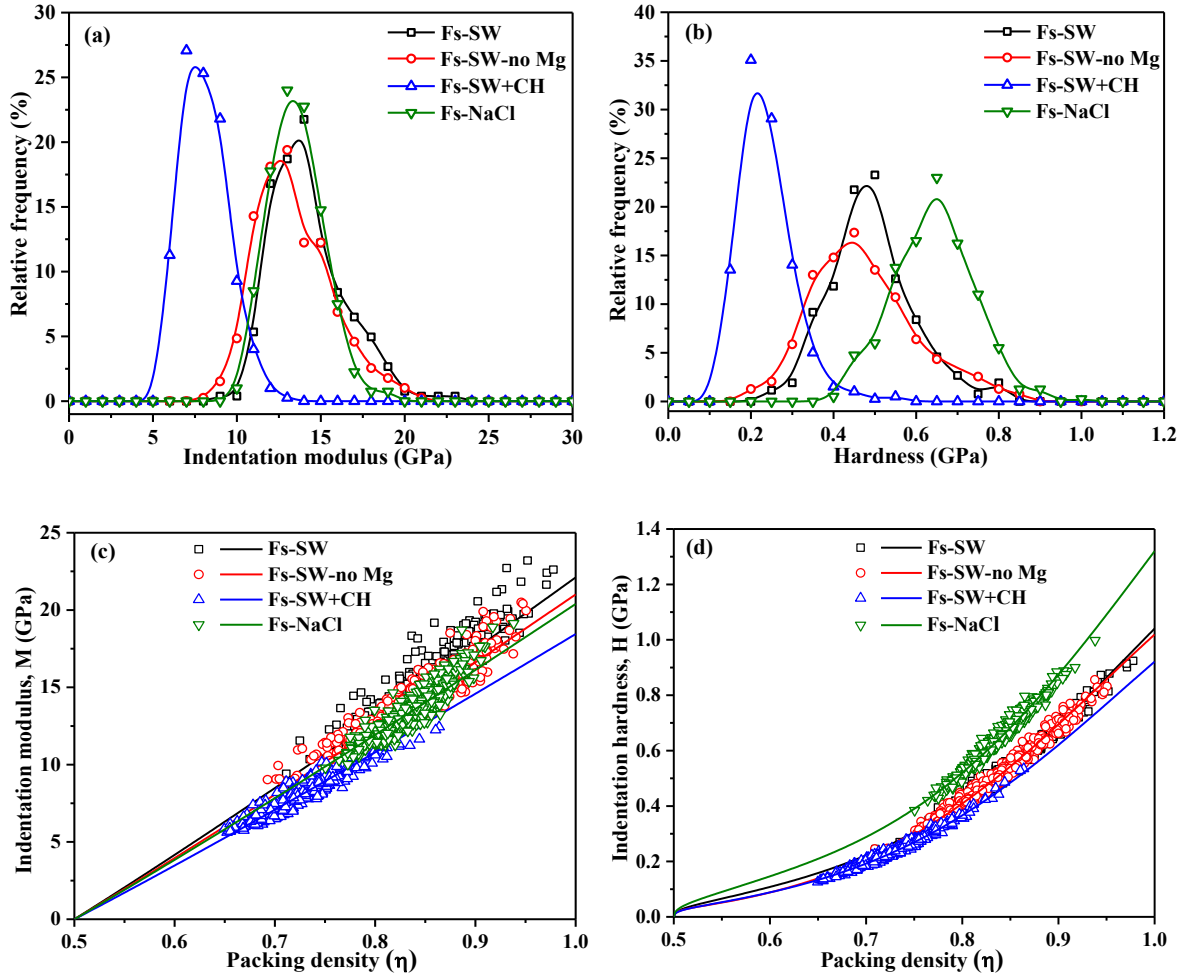

Fig. 6 Frequency plots of indentation modulus (a) and hardness (b) for the synthetic different Friedel's salt. Scaling relations of indentation modulus (c) and hardness (d) with the packing density of these Friedel's salt samples as calculated by the nanoindentation data.

Table 4 Mean packing density (Mean η), intrinsic stiffness (m_s), and intrinsic hardness (h_s) for the synthetic Friedel's salt samples.

Sample ID	Mean η (%)	m_s (GPa)	h_s (GPa)
Fs-SW	0.84	22.11	1.04
Fs-SW-no Mg	0.82	21.01	1.03
Fs-SW+CH	0.73	18.45	0.92
Fs-NaCl	0.84	20.39	1.32

3.2.4 Elemental composition

Based on the BSE measurement, the elemental composition of Friedel's salt formed in different solutions is shown in Fig. 7. It can be seen from the Al/Ca ratio in Fig. 7 (a) that the Fs-SW, Fs-SW-no Mg and Fs-NaCl samples had an Al/Ca ratio close to the ideal value of the Friedel's salt, *i.e.*, ~ 0.5. By contrast, the Fs-SW+CH sample had a relatively higher Al/Ca ratio, which was ascribed to a relatively lower Ca content after comparing the atomic percentages of Ca and Al in Fig. 7 (b). Considering that the Mg ions could also enter the Al^{3+}-hydroxides in the forming process of the Friedel's salt as described in Section 3.2.1, the Al/(Mg+Ca) ratios of different Friedel's salts are presented in Fig. 7 (c). Compared to other Friedel's salt samples, the Fs-SW+CH sample still had a relatively higher Al/(Mg+Ca) ratio, *i.e.*, a lower content of divalent ions.

Regarding the Cl/Ca ratio in Fig. 7 (a), compared with the Fs-NaCl sample, the Fs-SW, Fs-SW-no Mg, and Fs-SW+CH samples had a relatively lower Cl/Ca ratio. This could be attributed to the fact that, except for Cl^-, SO_4^{2-} in seawater also entered the interlayer structure of the Friedel's salt to balance the positive charges of the main layers ($[Ca_2Al(OH)_6]^+$) of the Friedel's salt [27, 44, 71]. The presence of S in the EDS results of Fs-SW, Fs-SW-no Mg, and Fs-SW+CH samples was also further supported the above proposition (Fig. 7 (d)). When the atomic percentages of S detected in the different Friedel's salt samples were equivalently converted to the corresponding Cl^- content (Fig. 7 (e)), it is noted that the $Cl_{equiv.}$/Ca ratio of the Fs-SW and Fs-SW+CH sample increased to the level of the Fs-NaCl sample. By contrast, there was still a relatively lower $Cl_{equiv.}$/Ca ratio for the Fs-SW-no Mg sample than the other Friedel's salt samples. This may be related to the relatively lower initial concentration of Cl^- in the Fs-SW-no Mg sample due to the exclusion of $MgCl_2$ in the preparation of the SW-no $MgCl_2$ solution. It has been reported that, within a specific range of the concentration of Cl^-, OH^- was

also inserted into the structure of Friedel's salt, and the amount would increase with the decrease of the concentration of Cl^-, which would lead to a relatively lower Cl/Ca ratio of the Friedel's salt [27]. This phenomenon is further illustrated in Fig. 7 (f): the Friedel's salt formed in the 12.4 mM NaCl solution had a lower Cl/Ca ratio than that formed in the 22.3 mM NaCl solution. The insertion of OH^- in the structure of Friedel's salt also explained why the $Cl_{equiv.}$/Ca ratios in the Fs-NaCl, Fs-SW, and Fs-SW+CH samples were lower than the theoretical value (Cl/Ca=0.5) (Fig. 7 (e)).

Furthermore, the Cl/Ca ratio of the Fs-SW+CH sample was almost comparable to that of the Fs-SW sample (Figs. 7 (a) and 7 (e)), even though a relatively lower amount of Ca was present in the Fs-SW+CH sample (Fig. 7 (b)). Therefore, it can further be inferred that a relatively small amount of Cl^- could be bound in the interlayers of the Fs-SW+CH sample. This could be explained by the fact that a small amount of Ca^{2+} intercalated into the Al^{3+}-hydroxides would result in relatively fewer positive charges of the principal layers. Consequently, less anions would be inserted into the interlayers to balance the charge.

In summary, at the concentration level of Cl^- in seawater, *i.e.*, 0.56 mol/L, the formed Friedel's salt was not a pure phase, but a solid solution containing [Cl, OH, SO_4] in its interlayer structure. But the amount of OH^- and SO_4^{2-} incorporated into the Friedel's salt formed in seawater was too limited to change the crystal structure as depicted in XRD data (Fig. S2 (a) in the supplementary material). When other cement hydrates, *e.g.*, portlandite, were present in the seawater system, the Friedel's salt formed had a relatively lower content of divalent ions to reduce the positive charges carried by the host layers of the Friedel's salt. Meanwhile, a lesser amount of Cl^- would be bound in its interlayer structure of the Friedel's salt to balance the charge.

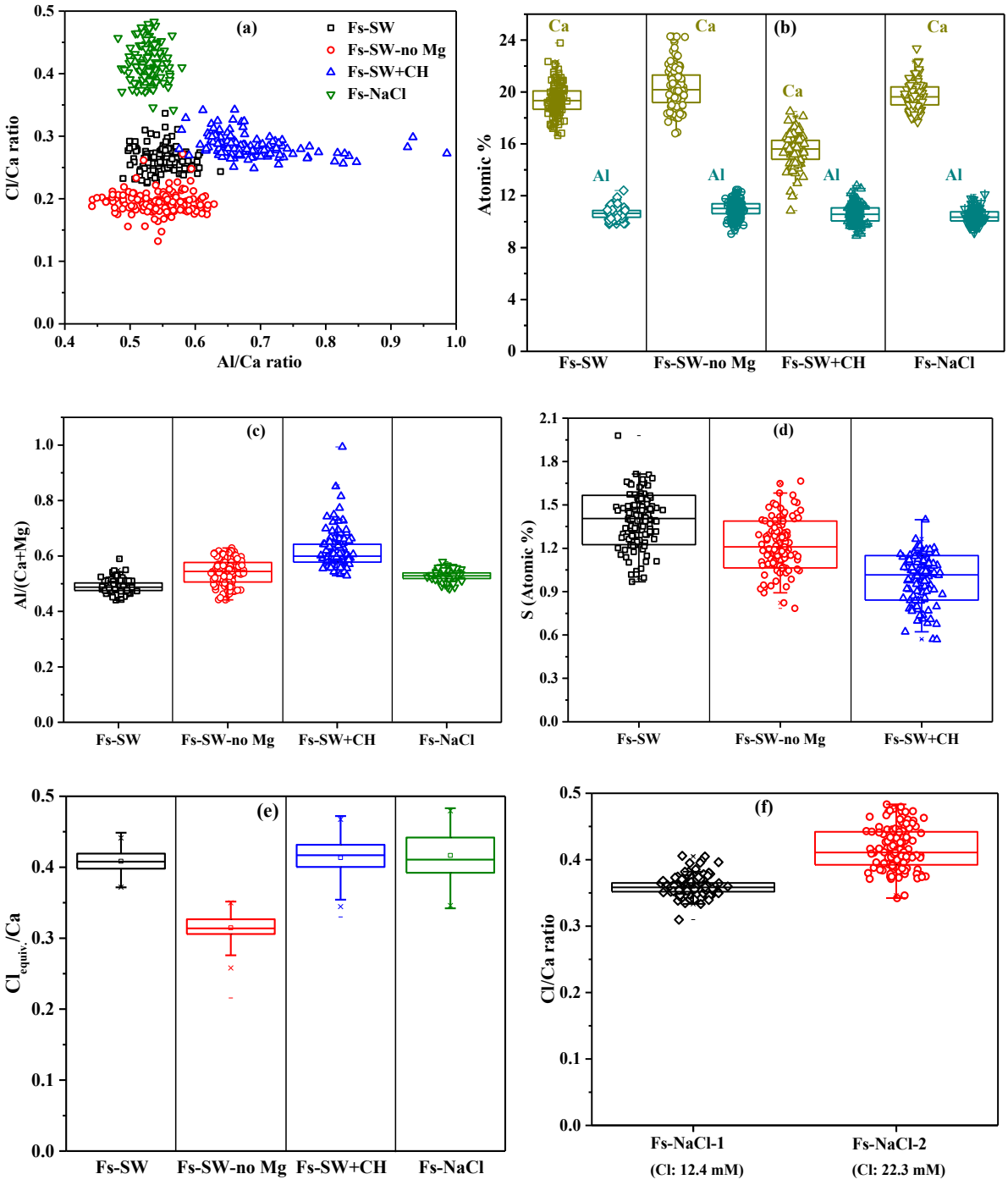

Fig. 7 Elemental composition analysis of synthetic Friedel's salt samples in different solutions. (a) is the Al/Ca ratio and Cl/Ca ratio. (b) is the atomic percentage of Ca and Al. (c) is the Al/(Ca+Mg) ratio. (d) is the atomic percentage of S. (e) is the $Cl_{equiv.}$/Ca ratio, and the $Cl_{equiv.}$ means that the atomic percentage of SO_4^{2-} detected was equivalently converted to the atomic percentage of Cl^-, *i.e.*, $Cl_{equiv.}=(Cl+S\times2)$. In other words, when one SO_4^{2-} was inserted into the interlayer of Friedel's salt, it would occupy two Cl^- sites according to the charge balance. (f) is

the Cl/Ca ratio of the Fs-NaCl samples synthesized in different concentrations of NaCl solutions.

3.2.5 Structural and compositional defects in Friedel's salt

To explore the influence of structural and compositional defects on the elastic properties of Friedel's salt, the elastic moduli of the Friedel's salt with Mg substitutions, Ca ion vacancies, and combined defects were calculated using molecular dynamics simulations (Fig. 8). The calculated bulk and shear moduli of the pure Friedel's salt were ~20 GPa and 12.7 GPa, respectively, which were comparable to the reported results [26].

According to the EDS data in Fig. 9, Friedel's salt samples formed in seawater contained approximately 10 at.% of Mg-doped amount. It is noted that from Fig. 8, when 10 at.% Mg was incorporated into the structure of Friedel's salt, the bulk, shear, Young's moduli and Poisson's ratio barely changed within the error range. This illustrated that, replacing 10 at.% Ca with Mg, which had a relatively smaller atomic radius, did not significantly impact the elastic properties of Friedel's salt. By contrast, the Ca vacancies significantly increased the bulk modulus while decreasing the shear modulus, which decreased the Young's modulus and increased the Poisson's ratio, based on the theorem of elastic mechanics [72]. The decrease of Young's modulus was enhanced as the content of Ca vacancies increased from 5 at.% to 10 at.%. This further inferred that the presence of Ca vacancies in Friedel's salt could lead to the decrease of indentation modulus in Fig. 6. Furthermore, it was observed that the Friedel's salt with both Ca vacancies and Mg substitutions was less affected compared to that with Ca vacancies alone, which suggested that the Mg substitutions could mitigate the influence of Ca vacancies on the elastic properties of Friedel's salt to some extent.

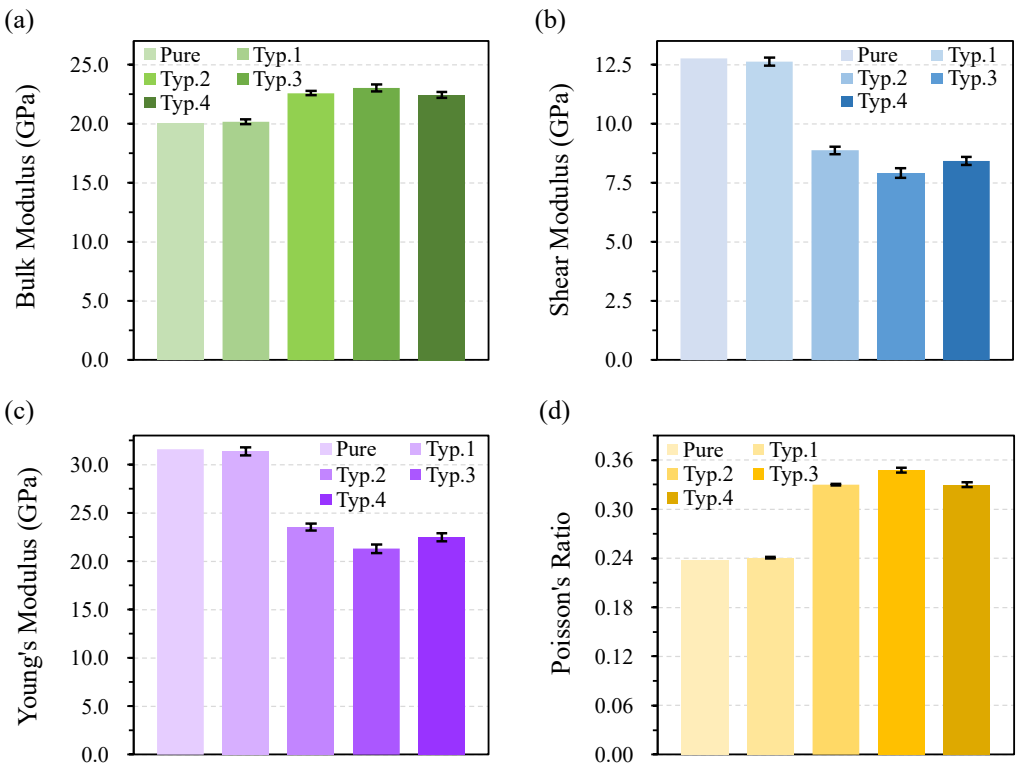

Fig. 8 Calculated (a) bulk modulus, (b) shear modulus, (c) Young's modulus, and (d) Poisson's ratio of different LDH phases. Pure: the pure Friedel's salt; Typ.1: the Friedel's salt with 10 at.% Ca substituted by Mg; Typ.2: the Friedel's salt with 5 at.% Ca vacancies; Typ.3: the Friedel's salt with 10 at.% Ca vacancies; Typ.4: the Friedel's salt with 10 at.% Ca vacancies and 5 at.% Ca substituted by Mg.

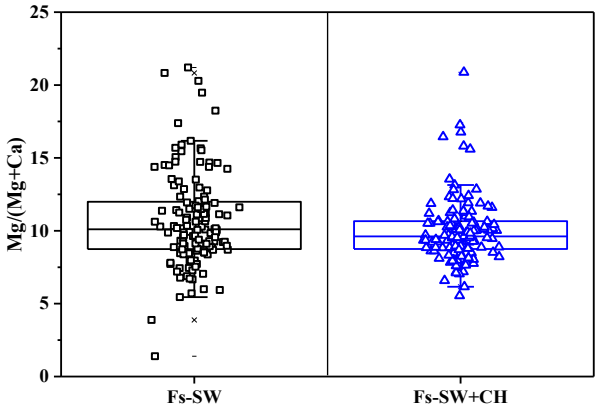

Fig. 9 Mg-doped amount in the Fs-SW and Fs-SW+CH samples. The atomic percentage of Mg and Ca was used to calculate the ratio of Mg/(Mg+Ca).

3.2.6 Discussion on Friedel's salt formed in seawater

The Friedel's salt formed in seawater is a solid solution, and anions like Cl^-, SO_4^{2-} and OH^- would be bound in its interlayer (Section 3.2.4). The insertion of a small amount of SO_4^{2-} (0.03 mol/L) in the interlayers of the Friedel's salt had a slight effect on the indentation modulus but decreased its hardness (the Fs-SW sample *vs*. the Fs-NaCl sample in Fig. 6). But when subjected to sulphate attack, Friedel's salt would be progressively converted into ettringite through the substitution of Cl^- by SO_4^{2-} [73], which might increase the indentation modulus and decrease the hardness of the matrix accordingly (Fig. 3). Besides, the amount of bound OH^- in the Friedel's salt was highly dependent on the initial Cl-concentration in the solution [27], Specifically, a lower concentration of Cl^- resulted in a higher contents of OH^- being incorporated into the Friedel's salt (Fig. 7 (f)). Also, the Friedel's salt sample with a lesser amount of OH^- exhibited a slightly higher indentation modulus and hardness (Fig. S6 in the supplementary material). This also further explained why the Fs-SW-no Mg sample had marginally lower micromechanical properties than the Fs-SW sample (Fig. 6).

Compared to the other Friedel's salt samples, the Fs-SW+CH sample formed in the solution with a higher concentration of OH^- exhibited the smallest particle size (Fig. 5 and Fig. S5). The reduction in the lateral-to-longitudinal ratio of LDH phases had been reported as an effective and simple way to introduce atomic vacancy defects [74], which could lead to a lower Ca content in the host layers of the Friedel's salt to increase its Al/Ca ratio (Figs. 7 (a)- 7 (c)). A similar result was also reported in Ref. [75]: the smaller LDH nanosheets exhibited a relatively higher ratio of trivalent cation-to-divalent cation (M^{3+}/M^{2+}), and vice versa. Taking into account the possibility that the Mg ions could be inserted into the main layer of Friedel's salt in the Fs-SW+CH sample, but its M^{3+}/M^{2+} ratio, *i.e.*, Al/(Mg+Ca), was still higher than the theoretical value, *i.e.*, the presence of Ca vacancies (Fig. 7 (c)). After conducting molecular dynamics simulations, the Ca vacancies in the structure of the Fs-SW+CH crystals could be

responsible for the decrease of Young's modulus (Fig. 8), rendering the decline of indentation modulus (Fig. 6).

4 Practical implication

In real cementitious materials, the SO_4-AFm phase is commonly found intermixed with the C-S-H gel [76-78]. Thus, when the nanoindentation test was applied in the heterogenous cementitious system, it is very difficult to accurately differentiate every single phase, e.g., the SO_4-AFm phase, because the overlapping values of modulus and hardness among different phases and the relatively small amount found in the real cement paste. Therefore, the nanoindentation study on the single phase is essential to further understand the micromechanical properties of the complex cementitious system. In Portland cement, the impact of the SO_4-AFm phase on the micromechanical properties could be minimal owing to its low proportion within the total hydrates. However, when a large amount of supplementary cementitious materials (SCMs) containing richer amounts of active aluminate phases, *e.g.*, calcined clay, metakaolin, and certain types of fly ash and ground granulated blast furnace slag (GGBS), are added to the Portland cement, the amount of SO_4-AFm phase would significantly increase accordingly. If seawater is used as the mixing water, the formation of more SO_4-Cl-AFm or/and Cl-AFm phases instead of the SO_4-AFm phase might increase the intrinsic stiffness and hardness of the matrix. The strengthening of the AFm structure by incorporation of Cl would favor the improvement of the macro-mechanical properties of cementitious materials.

Furthermore, compared to the ions present in seawater, the alkalinity in the reaction system seems to have a relatively significant effect on the particle size, elemental composition, and micromechanical properties of Friedel's salt (Cl-AFm phase) formed. In the context of carbon neutrality, carbonation mixing [79] or/and carbonation curing techniques [80] are employed to

increase the CO_2 uptake in cement and concrete. The early carbonation would consume the portlandite formed. In this case, the absence of portlandite in the cementitious material might contribute to the formation of Friedel's salt with relatively higher micromechanical properties. However, the continuous carbonation curing of the cementitious materials could result in the phase transformation of Friedel's salt into hemicarboaluminate or monocarboaluminate and even calcium carbonate. The corresponding changes in the micromechanical properties also worths further studies.

5 Conclusions

In this work, the micromechanical properties of Cl-containing AFm and SO_4-containing AFm were first examined. Then the effects of ions present in seawater on the morphology, composition, and micromechanical properties of Cl-containing AFm (Friedel's salt) were investigated. The packing density calculations and molecular dynamics simulations were employed to analyse the micromechanical properties. The following main findings can be drawn:

- When the SO_4^{2-} in the interlayer of Ca-Al layered double hydroxide of the AFm structure was gradually replaced by Cl^-, the basal spacing of AFm crystals became shortened. This would increase their packing density and consequently increase the indentation modulus and hardness, *i.e.*, Cl-AFm (Friedel's salt) > SO_4-Cl-AFm (Kuzel's salt) > SO_4-AFm (monosulphate).
- The Friedel's salt formed in seawater contained [Cl^-, OH^-, SO_4^{2-}] in its interlayer structure. The amount of OH^- bounded in the Friedel's salt would increase with the decrease of Cl^- concentration, and the micromechanical property was also reduced accordingly. The insertion of SO_4^{2-} (0.03 mol/L in seawater) in the Friedel's salt seemed to have a negligible effect on its indentation modulus but decreased its hardness.

- When portlandite was incorporated into seawater, the Friedel's salt formed was of relatively small particle sizes with a larger Al/Ca ratio due to the presence of Ca vacancies. Molecular dynamics simulations indicated that the formation of Ca vacancies significantly decreased the Young's modulus of the nanocrystals of Friedel's salt, which could account for the decline in nanoindentation moduli in experiments. Additionally, molecular dynamics simulations suggested that the Mg substitution for Ca in the Friedel's salt barely changed the Young's modulus, which was consistent with the nanoindentation results.

Acknowledgements

The authors would like to thank the financial support of the Research Grants Council of the Hong Kong SAR Government (Project No. T22-502/18-R), the Research Centre for Resources Engineering towards Carbon Neutrality (RCRE), and The Hong Kong Polytechnic University.

Reference

[1] U. Ebead, D. Lau, F. Lollini, A. Nanni, P. Suraneni, T. Yu, A review of recent advances in the science and technology of seawater-mixed concrete, Cem. Concr. Res. 152 (2022) 106666.

[2] A. Ahmed, S. Guo, Z. Zhang, C. Shi, D. Zhu, A review on durability of fiber reinforced polymer (FRP) bars reinforced seawater sea sand concrete, Constr. Build. Mater. 256 (2020) 119484.

[3] F. Guo, S. Al-Saadi, R.S. Raman, X. Zhao, Durability of fiber reinforced polymer (FRP) in simulated seawater sea sand concrete (SWSSC) environment, Corros. Sci. 141 (2018) 1-13.

[4] Z. Wang, X.-L. Zhao, G. Xian, G. Wu, R.S. Raman, S. Al-Saadi, A. Haque, Long-term durability of basalt-and glass-fibre reinforced polymer (BFRP/GFRP) bars in seawater and sea sand concrete environment, Constr. Build. Mater. 139 (2017) 467-489.

[5] Y. Sun, Y. Zhang, Y. Cai, W.L. Lam, J.-X. Lu, P. Shen, C.S. Poon, Mechanisms on accelerating hydration of alite mixed with inorganic salts in seawater and characteristics of hydration products, ACS Sustain. Chem. Eng. 9 (2021) 10479-10490.

[6] Y. Cai, D. Xuan, C.S. Poon, Influence of availability of calcium on the hydration of tricalcium aluminate (C_3A) in seawater mixed C_3A-gypsum system, J. Am. Ceram. Soc. 105 (2022) 5895-5910.

[7] Y. Sun, J.-X. Lu, P. Shen, C.S. Poon, Hydration kinetics and microstructure evolution of NaCl-mixed tricalcium silicate pastes, Cem. Concr. Res. 161 (2022) 106934.
[8] Y. Cai, Y. Tao, D. Xuan, Y. Sun, C.S. Poon, Effect of seawater on the morphology, structure, and properties of synthetic ettringite, Cem. Concr. Res. 163 (2023) 107034.
[9] J. Wang, E. Liu, L. Li, Multiscale investigations on hydration mechanisms in seawater OPC paste, Constr. Build. Mater. 191 (2018) 891-903.
[10] P. Sikora, K. Cendrowski, M. Abd Elrahman, S.-Y. Chung, E. Mijowska, D. Stephan, The effects of seawater on the hydration, microstructure and strength development of Portland cement pastes incorporating colloidal silica, Appl. Nanosci. 10 (2020) 2627-2638.
[11] Y. Zhang, Y. Sun, H. Zheng, Y. Cai, W.L. Lam, C.S. Poon, Mechanism of strength evolution of seawater OPC pastes, Adv. Struct. Eng. 24 (2021) 1256-1266.
[12] P. Li, W. Li, T. Yu, F. Qu, V.W. Tam, Investigation on early-age hydration, mechanical properties and microstructure of seawater sea sand cement mortar, Constr. Build. Mater. 249 (2020) 118776.
[13] A. Younis, U. Ebead, P. Suraneni, A. Nanni, Fresh and hardened properties of seawater-mixed concrete, Constr. Build. Mater. 190 (2018) 276-286.
[14] H.Y. Ghorab, M. Hilal, A.J.C. Antar, Effect of mixing and curing waters on the behaviour of cement pastes and concrete Part 2: Properties of cement paste and concrete, Cem. Concr. Res. 20 (1990) 69-72.
[15] M. Etxeberria, A. Gonzalez-Corominas, P. Pardo, Influence of seawater and blast furnace cement employment on recycled aggregate concretes' properties, Constr. Build. Mater. 115 (2016) 496-505.
[16] L.G. Li, X.Q. Chen, S.H. Chu, Y. Ouyang, A.K.H. Kwan, Seawater cement paste: Effects of seawater and roles of water film thickness and superplasticizer dosage, Constr. Build. Mater. 229 (2019) 116862.
[17] Z. Hussain, N.M. Noor, M.A. Caronge, Workability and Compressive Strength of Seawater-Mixed Concrete Containing Rice Husk Ash as Supplementary Cementitious Material, Int. J. Integr. Eng. 11 (2019) 192-200.
[18] W.L. Lam, P. Shen, Y. Cai, Y. Sun, Y. Zhang, C.S. Poon, Effects of seawater on UHPC: Macro and microstructure properties, Constr. Build. Mater. 340 (2022) 127767.
[19] J. Xiao, C. Qiang, A. Nanni, K. Zhang, Use of sea-sand and seawater in concrete construction: Current status and future opportunities, Constr. Build. Mater. 155 (2017) 1101-1111.
[20] M.J. Sánchez-Herrero, A. Fernández-Jiménez, A. Palomo, C_3S and C_2S hydration in the presence of Na_2CO_3 and Na_2SO_4, J. Am. Ceram. Soc. 100 (2017) 3188-3198.
[21] B. Mota, T. Matschei, K. Scrivener, The influence of sodium salts and gypsum on alite hydration, Cem. Concr. Res. 75 (2015) 53-65.
[22] O. Mendoza, C. Giraldo, S.S. Camargo Jr, J.I. Tobón, Structural and nano-mechanical properties of Calcium Silicate Hydrate (CSH) formed from alite hydration in the presence of sodium and potassium hydroxide, Cem. Concr. Res. 74 (2015) 88-94.

[23] Y. Sun, J.-X. Lu, C.S. Poon, Strength degradation of seawater-mixed alite pastes: an explanation from statistical nanoindentation perspective, Cem. Concr. Res. 152 (2022) 106669.
[24] M. Harris, G. Simpson, K. Scrivener, P. Bowen, A method for the reliable and reproducible precipitation of phase pure high Ca/Si ratio (> 1.5) synthetic calcium silicate hydrates (CSH), Cem. Concr. Res. 151 (2022) 106623.
[25] G. Paul, E. Boccaleri, L. Buzzi, F. Canonico, D. Gastaldi, Friedel's salt formation in sulfoaluminate cements: a combined XRD and ^{27}Al MAS NMR study, Cem. Concr. Res. 67 (2015) 93-102.
[26] T. Honorio, H. Carasek, O. Cascudo, Friedel's salt: Temperature dependence of thermoelastic properties, Cem. Concr. Res. 160 (2022) 106904.
[27] U. Birnin-Yauri, F. Glasser, Friedel's salt, $Ca_2Al(OH)_6(Cl,OH)\cdot 2H_2O$: its solid solutions and their role in chloride binding, Cem. Concr. Res. 28 (1998) 1713-1723.
[28] Y. Cai, D. Xuan, P. Hou, J. Shi, C.S. Poon, Effect of seawater as mixing water on the hydration behaviour of tricalcium aluminate, Cem. Concr. Res. 149 (2021) 106565.
[29] P. Li, W. Li, Z. Sun, L. Shen, D. Sheng, Development of sustainable concrete incorporating seawater: A critical review on cement hydration, microstructure and mechanical strength, Cem. Concr. Compos. 121 (2021) 104100.
[30] W.-J. Long, X. Zhang, G.-L. Feng, J. Xie, F. Xing, B. Dong, J. Zhang, K.H. Khayat, Investigation on chloride binding capacity and stability of Friedel's salt in graphene oxide reinforced cement paste, Cem. Concr. Compos. 132 (2022) 104603.
[31] Y. Elakneswaran, T. Nawa, K. Kurumisawa, Electrokinetic potential of hydrated cement in relation to adsorption of chlorides, Cem. Concr. Res. 39 (2009) 340-344.
[32] J. Wang, J. Xie, Y. Wang, Y. Liu, Y. Ding, Rheological properties, compressive strength, hydration products and microstructure of seawater-mixed cement pastes, Cem. Concr. Compos. 114 (2020) 103770.
[33] H. Li, N. Farzadnia, C. Shi, The role of seawater in interaction of slag and silica fume with cement in low water-to-binder ratio pastes at the early age of hydration, Constr. Build. Mater. 185 (2018) 508-518.
[34] T.U. Mohammed, H. Hamada, T. Yamaji, Performance of seawater-mixed concrete in the tidal environment, Cem. Concr. Res. 34 (2004) 593-601.
[35] A. Suryavanshi, J. Scantlebury, S. Lyon, Pore size distribution of OPC & SRPC mortars in presence of chlorides, Cem. Concr. Res. 25 (1995) 980-988.
[36] J. Xiao, Q. Zhang, P. Zhang, L. Shen, C. Qiang, Mechanical behavior of concrete using seawater and sea-sand with recycled coarse aggregates, Struct. Concr. 20 (2019) 1631-1643.
[37] A. Standard, D1141-98: Standard Practice for the Preparation of Substitute Ocean Water, ASTM International, West Conshohocken, 2013.
[38] M. Miller, C. Bobko, M. Vandamme, F.-J. Ulm, Surface roughness criteria for cement paste nanoindentation, Cem. Concr. Res. 38 (2008) 467-476.

[39] L.G. Baquerizo, T. Matschei, K.L. Scrivener, M. Saeidpour, A. Thorell, L. Wadsö, Methods to determine hydration states of minerals and cement hydrates, Cem. Concr. Res. 65 (2014) 85-95.
[40] S. Speziale, F. Jiang, Z. Mao, P.J. Monteiro, H.-R. Wenk, T.S. Duffy, F.R. Schilling, Single-crystal elastic constants of natural ettringite, Cem. Concr. Res. 38 (2008) 885-889.
[41] M. Vandamme, F.-J. Ulm, Nanoindentation investigation of creep properties of calcium silicate hydrates, Cem. Concr. Res. 52 (2013) 38-52.
[42] T.I. Bruker, in: Premier User Manual, 2018, pp. 173-175.
[43] F.J. Ulm, M. Vandamme, C. Bobko, J. Alberto Ortega, K. Tai, C. Ortiz, Statistical indentation techniques for hydrated nanocomposites: concrete, bone, and shale, J. Am. Ceram. Soc. 90 (2007) 2677-2692.
[44] J.-P. Rapin, G. Renaudin, E. Elkaim, M. Francois, Structural transition of Friedel's salt $3CaO{\cdot}Al_2O_3{\cdot}CaCl_2{\cdot}10H_2O$ studied by synchrotron powder diffraction, Cem. Concr. Res. 32 (2002) 513-519.
[45] R. Hill, The elastic behaviour of a crystalline aggregate, Proc. Phys. Soc. A, 65 (1952) 349.
[46] A.P. Thompson, H.M. Aktulga, R. Berger, D.S. Bolintineanu, W.M. Brown, P.S. Crozier, P.J. in't Veld, A. Kohlmeyer, S.G. Moore, T.D. Nguyen, LAMMPS-a flexible simulation tool for particle-based materials modeling at the atomic, meso, and continuum scales, Comput. Phys. Commun. 271 (2022) 108171.
[47] S. Plimpton, Fast parallel algorithms for short-range molecular dynamics, J. Comput. Phys. 117 (1995) 1-19.
[48] T. Honorio, P. Guerra, A. Bourdot, Molecular simulation of the structure and elastic properties of ettringite and monosulfoaluminate, Cem. Concr. Res. 135 (2020) 106126.
[49] M. Balonis, B. Lothenbach, G. Le Saout, F.P. Glasser, Impact of chloride on the mineralogy of hydrated Portland cement systems, Cem. Concr. Res. 40 (2010) 1009-1022.
[50] M.Y. Kiriukhin, K.D. Collins, Dynamic hydration numbers for biologically important ions, Biophys. Chem. 99 (2002) 155-168.
[51] F. Georget, B. Lothenbach, W. Wilson, F. Zunino, K.L. Scrivener, Stability of hemicarbonate under cement paste-like conditions, Cem. Concr. Res. 153 (2022) 106692.
[52] M.J. Abdolhosseini Qomi, F.J. Ulm, R.J.M. Pellenq, Evidence on the dual nature of aluminum in the calcium-silicate-hydrates based on atomistic simulations, J. Am. Ceram. Soc. 95 (2012) 1128-1137.
[53] R. Shahsavari, M.J. Buehler, R.J.M. Pellenq, F.J. Ulm, First-principles study of elastic constants and interlayer interactions of complex hydrated oxides: Case study of tobermorite and jennite, J. Am. Ceram. Soc. 92 (2009) 2323-2330.
[54] C. Dharmawardhana, A. Misra, S. Aryal, P. Rulis, W. Ching, Role of interatomic bonding in the mechanical anisotropy and interlayer cohesion of CSH crystals, Cem. Concr. Res. 52 (2013) 123-130.
[55] X. Yue, W. Liu, Z. Chen, Z. Lin, Simultaneous removal of Cu (II) and Cr (VI) by Mg–Al–Cl layered double hydroxide and mechanism insight, J. Environ. Sci. 53 (2017) 16-26.

[56] R. Rojas, Copper, lead and cadmium removal by Ca Al layered double hydroxides, Appl. Clay Sci. 87 (2014) 254-259.
[57] M.A. Yazdi, E. Gruyaert, K. Van Tittelboom, N. De Belie, New findings on the contribution of Mg-Al-NO_3 layered double hydroxides to the hydration and chloride binding capacity of cement pastes, Cem. Concr. Res. 163 (2023) 107037.
[58] H.F. Taylor, Cement Chemistry, 1997, pp. 182-186.
[59] P.K. Mehta, Effect of lime on hydration of pastes containing gypsum and calcium aluminates or calcium sulfoaluminate, J. Am. Ceram. Soc. 56 (1973) 315-319.
[60] R. Chitrakar, Y. Makita, A. Sonoda, T. Hirotsu, Synthesis of a novel layered double hydroxides $[MgAl_4(OH)_{12}](Cl)_2 \cdot 2.4H_2O$ and its anion-exchange properties, J. Hazard. Mater. 185 (2011) 1435-1439.
[61] Y. Yue, J.J. Wang, P.M. Basheer, Y. Bai, Raman spectroscopic investigation of Friedel's salt, Cem. Concr. Compos. 86 (2018) 306-314.
[62] W. Wu, Y. Wu, T. Wang, D. Wang, Q. Gu, B. Jin, HCl removal using calcined Ca–Mg–Al layered double hydroxide in the presence of CO_2 at medium–high temperature, Catalysts, 10 (2019) 22.
[63] C.V. Luengo, M.A. Volpe, M.J. Avena, High sorption of phosphate on Mg-Al layered double hydroxides: Kinetics and equilibrium, J. Environ. Chem. Eng. 5 (2017) 4656-4662.
[64] F. Labajos, V. Rives, M. Ulibarri, Effect of hydrothermal and thermal treatments on the physicochemical properties of Mg-Al hydrotalcite-like materials, J. Mater. Sci. 27 (1992) 1546-1552.
[65] F. Millange, R.I. Walton, D. O'Hare, Time-resolved in situ X-ray diffraction study of the liquid-phase reconstruction of Mg–Al–carbonate hydrotalcite-like compounds, J. Mater. Chem. 10 (2000) 1713-1720.
[66] N. Mao, C.H. Zhou, J. Keeling, S. Fiore, H. Zhang, L. Chen, G.C. Jin, T.T. Zhu, D.S. Tong, W.H. Yu, Tracked changes of dolomite into Ca-Mg-Al layered double hydroxide, Appl. Clay Sci. 159 (2018) 25-36.
[67] Y. Zhao, F. Li, R. Zhang, D.G. Evans, X. Duan, Preparation of layered double-hydroxide nanomaterials with a uniform crystallite size using a new method involving separate nucleation and aging steps, Chem. Mater. 14 (2002) 4286-4291.
[68] S.K. Yun, T. Pinnavaia, Water content and particle texture of synthetic hydrotalcite-like layered double hydroxides, Chem. Mater. 7 (1995) 348-354.
[69] B.S. An, Y. Kwon, H.W. Cha, M.C. Kang, J.S. Oh, C.W. Yang, Quantification of crystallinity using zero-loss filtered electron diffraction, Microsc. Res. Techniq. 82 (2019) 39-46.
[70] M. Collepardi, G. Baldini, M. Pauri, M. Corradi, Tricalcium aluminate hydration in the presence of lime, gypsum or sodium sulfate, Cem. Concr. Res. 8 (1978) 571-580.
[71] G. Renaudin, F. Kubel, J.-P. Rivera, M. François, Structural phase transition and high temperature phase structure of Friedels salt, $3CaO \cdot Al_2O_3 \cdot CaCl_2 \cdot 10H_2O$, Cem. Concr. Res. 29 (1999) 1937-1942.

[72] X. Du, L. Jin, G. Ma, Macroscopic effective mechanical properties of porous dry concrete, Cem. Concr. Res. 44 (2013) 87-96.
[73] J. Geng, D. Easterbrook, L.-y. Li, L.-w. Mo, The stability of bound chlorides in cement paste with sulfate attack, Cem. Concr. Res. 68 (2015) 211-222.
[74] X. Bian, S. Zhang, Y. Zhao, R. Shi, T. Zhang, Layered double hydroxide-based photocatalytic materials toward renewable solar fuels production, InfoMat. 3 (2021) 719-738.
[75] Z. Chang, C. Wu, S. Song, Y. Kuang, X. Lei, L. Wang, X. Sun, Synthesis mechanism study of layered double hydroxides based on nanoseparation, Inorg. Chem. 52 (2013) 8694-8698.
[76] I. Richardson, G. Groves, The incorporation of minor and trace elements into calcium silicate hydrate (C S H) gel in hardened cement pastes, Cem. Concr. Res. 23 (1993) 131-138.
[77] S.-D. Wang, K.L. Scrivener, Hydration products of alkali activated slag cement, Cem. Concr. Res. 25 (1995) 561-571.
[78] W. Wilson, L. Sorelli, A. Tagnit-Hamou, Unveiling micro-chemo-mechanical properties of C–(A)–S–H and other phases in blended-cement pastes, Cem. Concr. Res. 107 (2018) 317-336.
[79] S. Monkman, M. MacDonald, R.D. Hooton, P. Sandberg, Properties and durability of concrete produced using CO_2 as an accelerating admixture, Cem. Concr. Compos. 74 (2016) 218-224.
[80] Z. He, Z. Li, Y. Shao, Effect of carbonation mixing on CO_2 uptake and strength gain in concrete, J. Mater. Civ. Eng. 29 (2017) 04017176.